

*Optimization of Cone-in-Shell Targets for an X-ray Backlighter on the National Ignition Facility*

**Anirudh Sharma**

Webster Schroeder High School

Advisor: Dr. R. S. Craxton

Laboratory for Laser Energetics

University of Rochester

November 2018

## 1. Abstract

A double cone-in-shell plastic (CH) target imploded by laser beams has been optimized for the purpose of x-ray backlighting a hohlraum-heated iron sample in an opacity platform at the National Ignition Facility (NIF). The cones, which are located at the poles of a spherical shell, allow the target to produce a short pulse of x rays that probe the sample at a specified time. Both the parameters of the available laser beams and specifications of the cones have been optimized using the 2D hydrodynamics simulation code *SAGE*. By placing all the beams in best focus and appropriately selecting the pointings of the beams, a uniform implosion has been achieved. The behavior of the cone has been optimized by selecting a sufficiently small cone half-angle that laser rays do not enter the cone and a sufficiently large distance from the cone tip to the target center that the cone's obstruction of the implosion is minimal. An x-ray diagnostic code, *Orion*, has been created for the purpose of calculating the x-ray output from the targets. The optimized design has been found to produce a short ( $\sim 350$  ps) point source ( $\sim 100$   $\mu\text{m}$ ) of x rays as desired, effectively eliminating emission produced by the target before peak compression ("run-in"). The parameters of the design are chosen to ensure that the convergence of the cone on the vertical axis prevents hot compressed plasma from escaping through the cone after peak compression. This design has also been compared to a conventional target lacking cones. Calculations from *Orion* have shown that the conventional target produces significant run-in emission and a longer x-ray pulse than the optimized cone-in-shell design. This work suggests that a double cone-in-shell target is a viable candidate for improved backlighting of opacity experiments at the NIF.

## 2. Introduction

### 2.1. Iron Opacity Experiments at the NIF

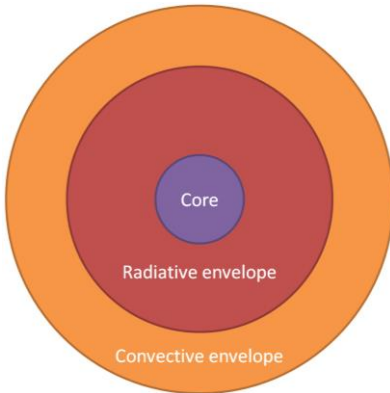


Figure 2.1: The radiative and convective zones of the sun. The transition radius between the two is unknown.

(a chamber made of a high-atomic-number material such as gold) and x rays emitted by the hohlraum wall heat an iron sample. Laser rays are also used to implode a backlighter target. The target in Fig. 2.2 (a) is a plastic (CH) shell, often known as a capsule. The imploded target is indicated with dotted lines in Fig. 2.2. The backlighter is intended to produce a short pulse of x rays. The proposed design [Fig. 2.2 (b)] uses a double cone-in-shell target instead of a conventional target.

In the sun, heat is transferred by two different methods: radiation and convection, as shown in Fig. 2.1. Currently, the transition radius, or the distance at which the method of heat transfer changes from radiation to convection, is unknown.

Experiments are being carried out to determine the opacity of iron, a value that the transition radius depends on. The current setup at the National Ignition Facility (NIF) at Lawrence Livermore National Laboratory for such experiments, designed by Heeter et al.,<sup>1</sup> is shown in Fig. 2.2 (a). The proposed setup, which is the focus of this work, is shown in Fig. 2.2 (b).

In both setups, laser rays heat the inner wall of a hohlraum

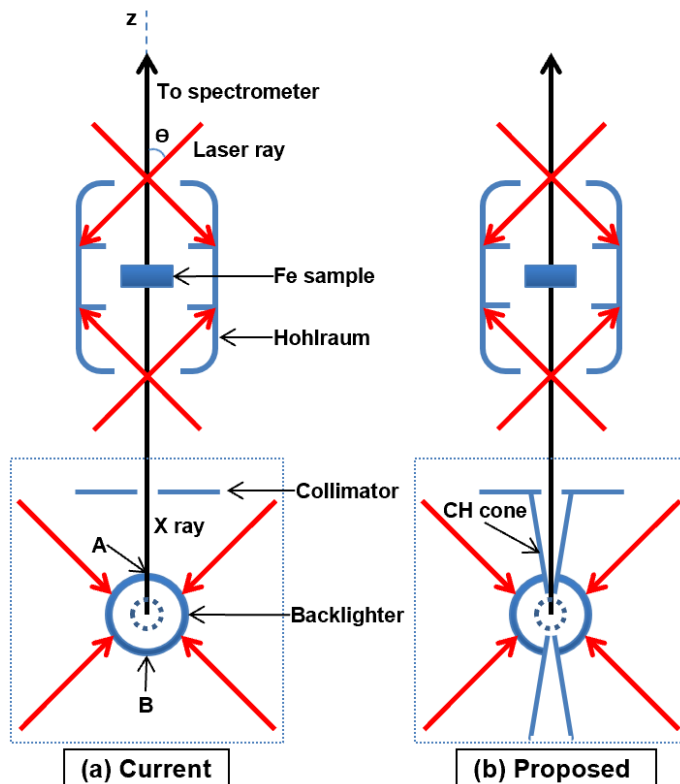


Figure 2.2: The current (a) and proposed (b) setups for the NIF Opacity Platform. In the proposed design (b), the conventional backlighter is replaced with a double cone-in-shell target.

X-ray emission from the backlighter is transmitted axially through a collimator and then through the hohlraum-heated iron sample (Fig. 2.3). The collimator is necessary to ensure that the sample's self-emission  $E$  (see Eq. 1) is measured without contamination from the backlighter x rays. At the spectrometer, different regions of emission can be used to determine the initial intensity of the emitted x rays, the final intensity, and the self-emission from the sample. Using the simple formula

$$T = \frac{U - E}{V - E} \quad (1)$$

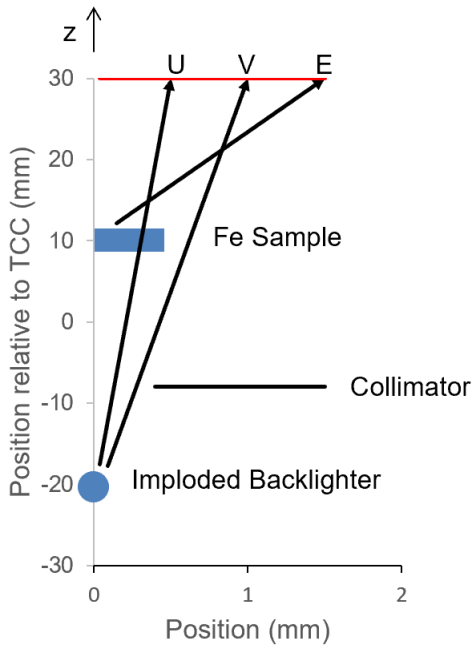


Figure 2.3: Regions of emission formed by the sample and backlighter. The spectrometer is located 600 mm from target chamber center (TCC). The horizontal scale has been greatly enlarged.

where  $T$  is the transmittance,  $U$  is the intensity in the direction of attenuated x rays that pass through the sample, and  $V$  is the intensity in the direction of unattenuated x rays that do not pass through the sample, the transmittance and thus the opacity of the heated sample can be found.<sup>1</sup> These regions of emission are shown in Fig. 2.3, which demonstrates how the sample's self-emission  $E$  contributes to the measurements of  $U$  and  $V$ , and consequently must be subtracted from both values to ensure an accurate transmittance calculation.

The backlighters in Fig. 2.2 are imploded using direct drive.<sup>2,3</sup> In direct drive implosions, a small spherical plastic capsule is irradiated with laser rays. As the laser rays heat the capsule, a layer of hot plasma (known as coronal plasma) forms around the capsule as the outer portion of the capsule ablates outward, causing an equal opposing force to drive the inner portion of the capsule inward. This process creates conditions of high temperature and pressure

in a small, compressed core. Such conditions lead to the emission of x rays.

The iron sample used in NIF opacity experiments is brought to solar-interior temperatures via indirect drive.<sup>4</sup> In indirect drive, the laser rays enter and heat a hohlraum, which contains the primary target. As the hohlraum is heated, it emits x rays, which then irradiate and heat the target.

Typically, there is a spherical capsule in the hohlraum that is imploded by these x rays. This implosion process, accomplished using either direct or indirect drive, is generally used for inertial confinement fusion (ICF). Capsules used for ICF are filled with deuterium-tritium fuel. High temperatures and densities provide the deuterium and tritium nuclei with sufficient energy to overcome

their Coulombic repulsion and fuse, producing a helium nucleus and a high-energy neutron. In the setup of Fig. 2.2, the iron sample is simply being heated rather than imploded as a target would be in ICF.

The NIF is configured for indirect drive, and the laser beams are arranged in rings of quads (where each quad has 4 beams) oriented at polar angles  $\Theta$  (indicated in Fig. 2.2) of  $23^\circ$ ,  $30^\circ$ ,  $45^\circ$ , and  $50^\circ$ . Indirect drive requires laser rays to enter through a hole at the top of the hohlraum; it is difficult to accomplish this using beams with  $\Theta > 50^\circ$ . Lasers configured for direct drive (such as the OMEGA laser<sup>5</sup> at the Laboratory for Laser Energetics) have beams oriented more uniformly around the entire target.

Only certain quads are available for the backlighter. The primary target is heated in the hohlraum by the  $45^\circ$  laser beams and the backlighter is driven by the  $23^\circ$  and  $30^\circ$  beams and every other  $50^\circ$  quad, as some of the  $50^\circ$  quads are blocked by the target holder.

While direct drive presents the obvious advantage of greater efficiency in energy deposition, indirect drive produces a smoother implosion in ICF and more consistent heating of a sample in opacity experiments. Direct drive can be accomplished at the NIF by repointing the laser beams toward the equator of the target, a process known as polar drive.<sup>6,7</sup> A similar repointing is done in this work in order to optimize the implosion of the backlighter.

## 2.2. Cone-in-Shell Backlighters

In current experiments at the NIF [Fig. 2.2 (a)], backlighters have presented the issue of “run-in,” or x-ray emission produced prior to peak compression as the laser rays continually heat the coronal plasma.<sup>8</sup> Such emission interferes with the transmittance measurements of the primary sample, as it creates a temporally spread signal which extends the duration of the spectrometer’s time-integrated measurements. Since the primary sample is evolving with time and it is desired to probe the sample at a specific time, this affects the accuracy of those measurements. While the collimator blocks much of this emission, run-in from regions A and B [Fig. 2.2 (a)] cannot be blocked as they directly view the sample. To resolve this issue, Heeter<sup>9</sup> proposed a double cone-in-shell target [Fig. 2.2 (b)]. The new capsule includes cones at both the poles that limit the view of the sample to a central region of the spherical backlighter capsule. Specifically, the design eliminates the portions of the shell in the polar regions A and B and thus the run-in from those areas. Consequently, there should be no detected emission until the capsule implodes, as there is no polar emission and the cone and collimator [Fig. 2.2 (b)] block the sample from run-in associated with the whole surface of the capsule.

Cone-in-shell targets have been fabricated for such applications as fast ignition,<sup>10</sup> but a double cone-in-shell target for the backlighting of opacity experiments, as explored in this work, is a new concept. This research proves that such a target is viable and may offer significant benefits over current capsules, especially in terms of producing a short-pulse signal.

The findings of this work are divided into three sections. In section 3, an initial cone-in-shell design that exhibits high uniformity is presented. In section 4, an x-ray diagnostic code *Orion* is developed and used to assess emission from the initial design. In section 5, an optimized design that produces a short pulse of x rays is shown and compared to current backlighters in use at the NIF.

### 3. Initial Design

Fig. 3.1 (a) shows the specifications for the initial cone-in-shell design. To develop this design, five parameters of the cone were investigated: length, distance from tip to target center, tip radius, thickness, and half-angle. The pointings and defocuses of the relevant beams ( $23^\circ$ ,  $30^\circ$  and  $50^\circ$ ) were varied as well. Fig. 3.1 (b) shows the laser pulse that was used to implode the target. The total laser energy is 300 kJ and 66.6% of the total energy is absorbed. The laser turns off at 2.8 ns.

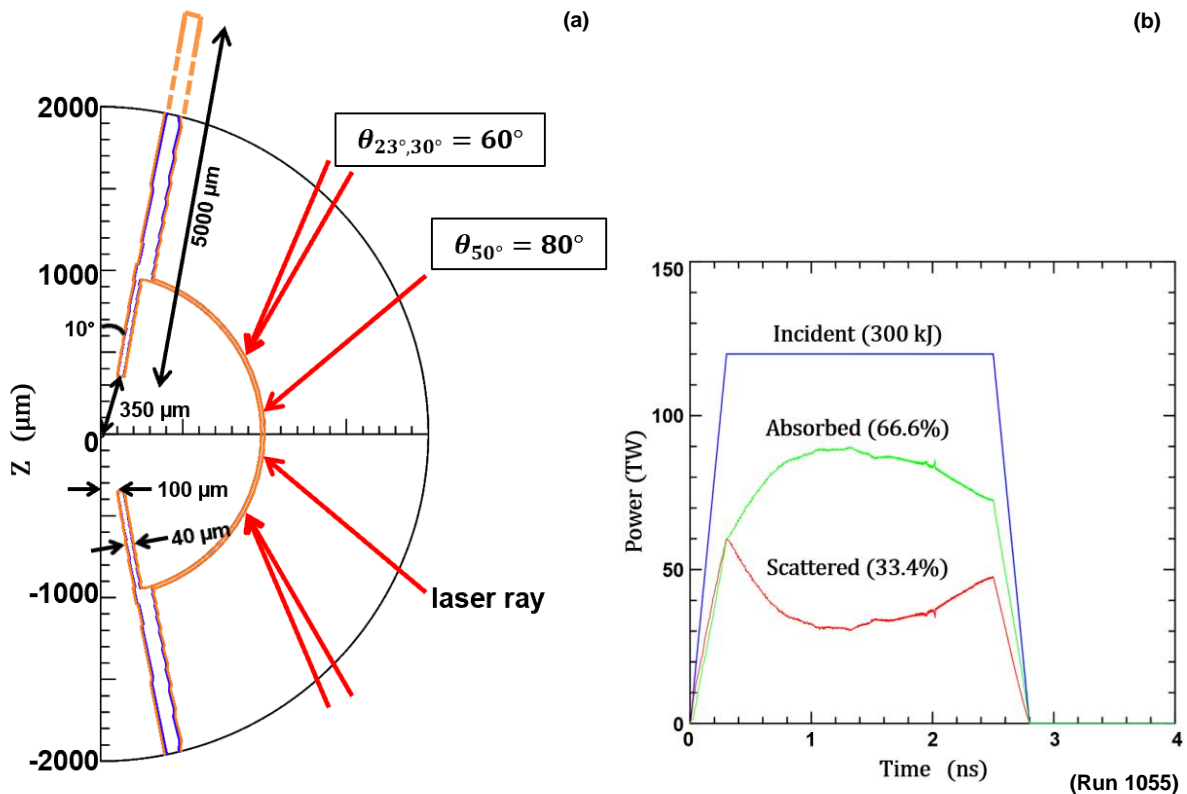


Figure 3.1: (a) The specifications for the initial cone-in-shell design and (b) plot of power versus time for the laser pulse used in all simulations. The red arrows indicate where the laser rays at the centers of the beams are aimed on the initial capsule surface.

These initial optimizations focused on preventing laser rays from entering the cone (which would cause the formation of unwanted radiating plasma inside the cone) and ensuring implosion uniformity, as this is necessary for achieving high densities and thus high x-ray output. It was found that  $10^\circ$  was a sufficiently small cone half-angle and 5000 μm was a sufficiently large cone length to prevent laser ray entry into the cone. In actual experiments, a greater length will be used since the cone must be mounted

on the collimator [Fig. 2.2 (b)]. A cone thickness of  $40\ \mu\text{m}$  was chosen to maintain the integrity of the cone during the implosion: a cone that is significantly thinner than  $40\ \mu\text{m}$  would collapse early and block x rays from the backlighter whereas a cone that is too thick limits the amount of shell material that can be driven inward during the implosion. A cone tip radius of  $100\ \mu\text{m}$  was selected to ensure that the imploded core would be in the view of the sample. For the distance from cone tip to target center,  $350\ \mu\text{m}$  was found to be large enough to not impede the implosion. The beam pointings were optimized to ensure adequate equatorial drive: the  $23^\circ$  and  $30^\circ$  beams were pointed at an angle of  $60^\circ$  on the initial target surface and the  $50^\circ$  beams were pointed at  $80^\circ$ . All of the beams were placed in best focus (which increased laser energy deposition at the equator), thereby achieving the desired uniformity.

The time evolution of the initial design is shown in Fig. 3.2, which shows electron-density contour plots at three times. The critical density (orange) is the highest density that laser rays can penetrate to. The initial design implodes with a high degree of uniformity, as clearly evidenced by the spherical appearance of the shell before and during peak compression. At  $1500\ \text{ps}$ , before the implosion, the shell (indicated by the concentrated blue contours) seems to be very uniformly driven across its entire surface. At  $2300\ \text{ps}$ , during the peak compression, the imploded core still appears spherical, suggesting a high-quality implosion. At  $3500\ \text{ps}$ , after the implosion, the plasma has expanded outward.

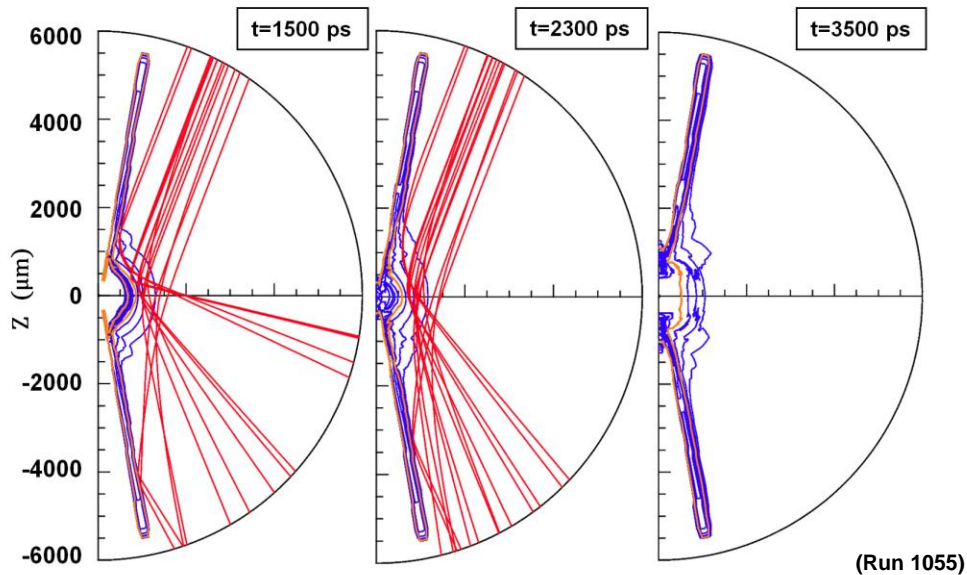


Figure 3.2: The time evolution of the initial cone-in-shell design. Incident laser rays are represented in red, and electron densities (of successive powers of  $1/2$  times the critical density) are indicated with blue contours (the critical density  $n_c$  is shown in orange). The shell implodes very uniformly.

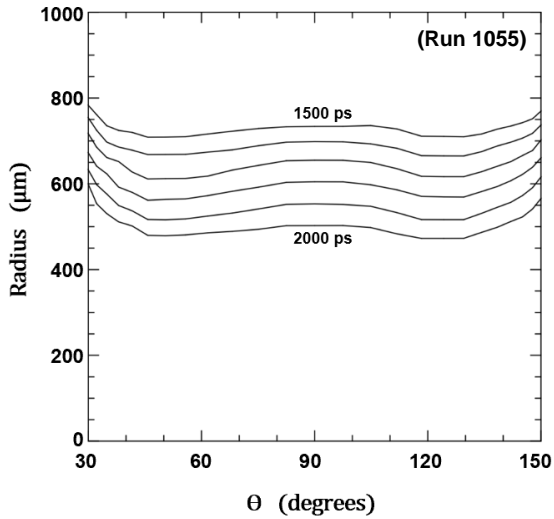


Figure 3.3: Center-of-mass radius plots superposed for 100 ps intervals from 1500 ps to 2000 ps. The implosion exhibits a high degree of uniformity.

A center-of-mass radius plot (for angles outside the range of the cone, where it can be defined) is shown in Fig. 3.3. The center-of-mass radius is the distance from the center of the target to the center of mass at some angle  $\theta$ . This plot shows that the center-of-mass radius is extremely consistent across the surface of the target leading up to the implosion. Both the time evolution plots of Fig. 3.2 and the center-of-mass radius plot show that the design exhibits a uniform implosion.

Blowups of the initial design (Fig. 3.4) reveal a new issue: hot compressed plasma escapes into the cone at late stages. The early appearance of this plasma is apparent at the time of implosion [Fig. 3.4 (a)], at which point compressed material already appears to be expanding along the axis. By 3000 ps [Fig. 3.4 (b)], the hot plasma has escaped further into the cone. The expansion of this hot plasma is indicated by the separation between the  $n_c$  and  $\frac{n_c}{2} - \frac{n_c}{8}$  contours. Due to the high temperatures and density of this material, it will emit x rays long after the implosion has ended, thus extending the x-ray pulse beyond what is desired.

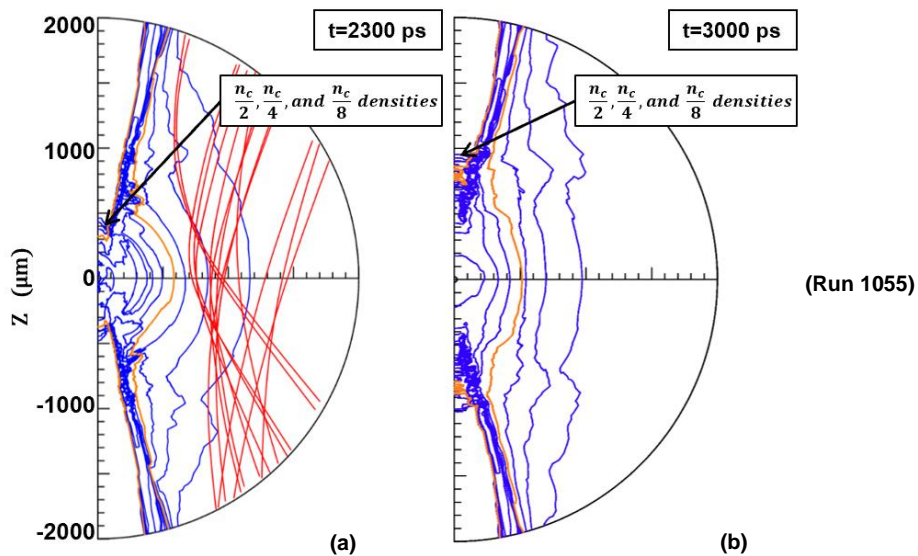


Figure 3.4: Density contour blowups for the initial design at the time of implosion (a) and after the implosion (b). Note the evolution of the expanding hot plasma in the cone as it escapes further up the axis.

Density contour plots (as in Fig. 3.2) show that the cone is pushed inward as the target implodes. If the cone continued to move inward, it would have converged onto the vertical axis, thus shutting off the x-ray signal. In the initial design, this did not occur due to the expanding hot plasma along the axis shown in Fig. 3.4.

It was found that if the cone is too thin, it will move at a greater velocity toward the axis, collapsing before peak central emission. Similarly, if the tip radius is too small, the convergence happens earlier than desired. A small tip radius also has the consequence of decreased output overall, as it limits the area of emission.

Other parameters, such as the distance from cone tip to target center and the beam pointings, affected the behavior of the cone as well, yet how they would affect x-ray emission was not completely clear. Since optimizing these features was dependent on how emission from the backlighter was distributed (both temporally and spatially), a code, *Orion*, was written to predict x-ray output from targets and aid in further optimizations.

#### 4. Development of X-ray Diagnostic Code

##### 4.1. The Code Orion

To diagnose a target that will be used as an x-ray backlighter, it is important to know how much emission it will produce. A simple differential equation can be used to find the intensity of an x ray as it passes through a radiating object.

The radiation transfer equation is given by

$$\frac{dI_\nu}{ds} = k'_\nu B_\nu - k'_\nu I_\nu \quad (2)$$

and is used here to model the spectral intensity of an x ray of frequency  $\nu$  traveling on a path through the plasma, where  $I_\nu$  is spectral intensity in  $\frac{\text{ergs}}{\text{sec} \times \text{cm}^2 \times \text{sr} \times \text{freq}}$ ,  $B_\nu$  is the blackbody spectral intensity,  $s$  is distance, and  $k'_\nu$  is opacity.<sup>11</sup> Note that there are both a positive term, which represents self-emission, and a negative term, which represents absorption. By starting with an x ray of zero intensity and calculating its spectral intensity as it passes through the capsule (growing due to self-emission and being attenuated due to absorption), the x-ray spectral intensity at a specific position and time can be determined.

The blackbody function  $B_\nu$  is given by

$$B_\nu = \frac{2h\nu^3}{c^2} \times \frac{1}{e^{\frac{h\nu}{k_B T}} - 1} \quad (3)$$

where  $h$  is Planck's constant,  $c$  is the speed of light,  $k_B$  is Boltzmann's constant, and  $T$  is temperature. For a given x-ray frequency, the blackbody intensity is solely a function of temperature.

By selecting a sufficiently small step  $ds$  that a constant temperature and thus an unchanging blackbody intensity, as well as a constant opacity, can be assumed along the step, the following relation is obtained from Eq. 2:

$$\frac{dI_\nu}{ds} = \frac{d(I_\nu - B_\nu)}{ds} = -k'_\nu(I_\nu - B_\nu) \quad (4)$$

Eq. 4 shows that  $I_\nu$  approaches  $B_\nu$ , regardless of whether  $I_\nu > B_\nu$  or  $I_\nu < B_\nu$ . The spectral intensity can be obtained as a function of position by integrating Eq. 4 to give  $I_\nu$  at a position that is an interval of  $ds$  greater than the original position  $s$ :

$$I_\nu(\mathbf{s} + d\mathbf{s}) = I_\nu(\mathbf{s})e^{-k'_\nu ds} + B_\nu(\mathbf{s})(1 - e^{-k'_\nu ds}) \quad (5)$$

Here, the absorption term is the first term on the right while the self-emission term is the second. The spectral intensity is decreased by a damping factor that depends on the opacity, and is increased by a term that depends on the blackbody value and the opacity.

An x-ray diagnostic code *Orion* was built using Fortran that models the spectral intensity of x-ray emission using this numerical integration technique. *Orion* can obtain solutions for Eq. 5 for single x rays and also calculate space and time integrals.

#### 4.2. X-ray Emission from the Initial Design

*Orion* can plot the intensity for an x ray as it passes through the target at some radius  $x$ . A simple example of this is shown in Fig. 4.1 for an imploded target. Two intensity plots are shown: that of an x ray passing unimpeded through the emitting center of the target (blue) as well as that of an x ray that experiences significant absorption upon reaching the optically thick cone (green). Here, intensity is plotted as  $\hat{I}_\nu$ , such that

$$\hat{I}_\nu = \frac{I_\nu}{h} \quad (6)$$

where  $h$  is Planck's constant. Since  $I_\nu$  is the spectral intensity in  $\frac{\text{ergs}}{\text{sec} \times \text{cm}^2 \times \text{sr} \times \text{freq}}$ ,  $\hat{I}_\nu$  is the spectral

intensity in  $\frac{\text{ergs}}{\text{sec} \times \text{cm}^2 \times \text{sr} \times \text{ergs}}$  (since the product  $h\nu$  gives energy in ergs), which is equivalent to

$\frac{1}{\text{sec} \times \text{cm}^2 \times \text{sr}}$ . In the figures presented here *Orion* plots are for an x-ray energy  $h\nu$  of 700 eV (which is in the range of interest for opacity measurements).

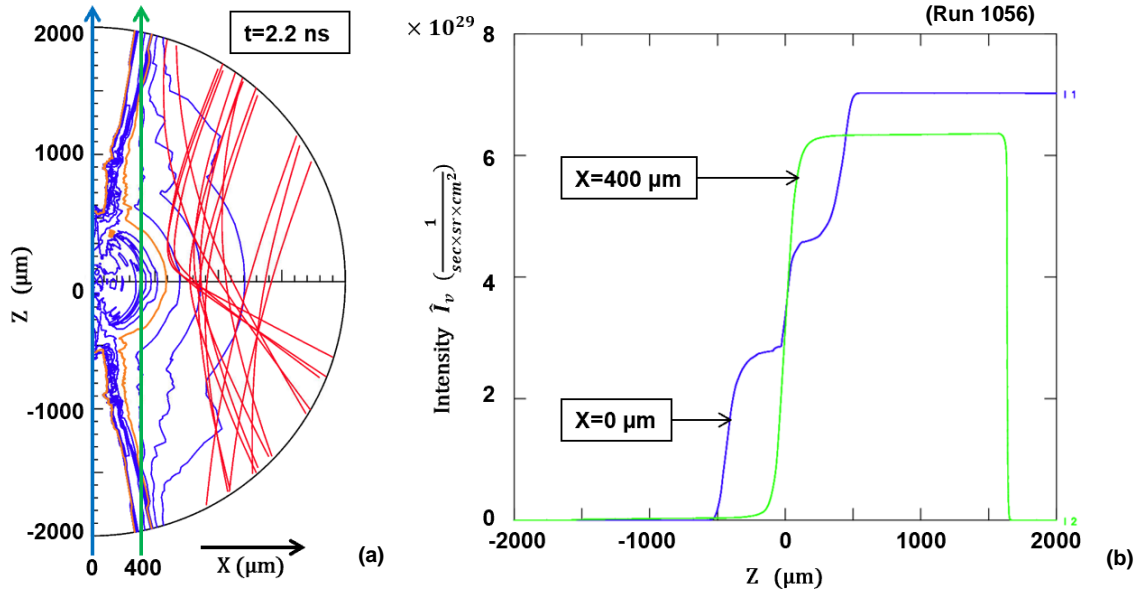


Figure 4.1: Density contour plot of an imploded target (a) and intensity lineouts produced by Orion at two radii (b). The paths of a ray through the center and one at a radius of  $400 \mu\text{m}$  are shown in (a). Their respective intensities as a function of their  $z$ -position are plotted in (b). Note the sharp attenuation of the ray at a radius of  $400 \mu\text{m}$  when it reaches the cone at  $z \sim 1500 \mu\text{m}$ .

The first ray, indicated in blue, increases in intensity as it passes through the hot plasma and the compressed core of the target, a region extending from approximately  $z = -500 \mu\text{m}$  to  $500 \mu\text{m}$ . The high temperature and density of this area cause the significant self-emission that is evidenced by the rise in spectral intensity in Fig. 4.1 (b). The second ray, indicated in green, also passes through a region of hot, compressed material, leading to a rise in intensity as it crosses the  $x$  axis; the green ray grows over a smaller range of  $z$ . Upon reaching the cone ( $z \sim 1500 \mu\text{m}$ ), the intensity is rapidly attenuated to virtually zero [Fig. 4.1 (b)]. This is caused by the high opacity and low temperature of the cone, which lead to low self-emission and high absorption.

The output intensity of x-ray emission can be spatially integrated at a given time over some circular region. Thus, the total emission at that time can be found, allowing the pulse duration to be determined. The space-integrated intensity is defined as

$$\int_0^{x_c} \hat{I}_v \cdot 2\pi x dx \quad (7)$$

where  $\hat{I}_v$  is the spectral intensity as previously defined and  $x_c$  is the radius of the collimator ( $400 \mu\text{m}$ ). Since the intensity is integrated over space, its units are  $\frac{1}{\text{sec} \times \text{sr}}$ .

A plot of space-integrated intensity versus time for the initial design is shown in Fig. 4.2. The effects of the hot plasma escaping into the cone [Fig. 3.4 (b)] are evident. The emission produced in the

initial design after peak compression, due to this hot plasma, far outstrips that produced during the actual implosion and causes an extended pulse. Note that the maximum is  $3.8 \times 10^{26} \frac{1}{\text{sec} \times \text{sr}}$  or  $61 \frac{\text{GW}}{\text{keV} \times \text{sr}}$ .

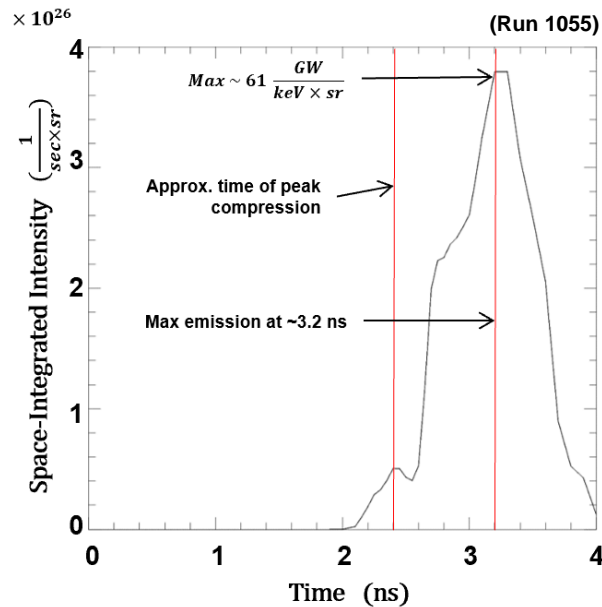


Figure 4.2: Plot of space-integrated intensity versus time for the initial design. Note that the maximum occurs long after the time of peak compression, significantly extending the duration of the pulse. This late-stage emission is caused by hot, emitting plasma that escaped into the cone (see Fig. 3.4)

*Orion* was used to guide the development of subsequent designs, which aimed to eliminate this late-stage emission in order to shorten the x-ray pulse.

## 5. Optimized Design

### 5.1. Improving the Initial Design

In the initial design, the inward movement of the cone was impeded by the expansion of hot compressed plasma. If the hot plasma had not flown out of the cone tip, the cone would have converged onto the vertical axis, thus preventing late-stage emission by sealing off the compressed material from view of the spectrometer. Later designs aimed to produce this convergence before imploded material could escape into the cone. *Orion* total emission (space-integrated intensity) plots against time were especially useful in diagnosing these designs, as they confirmed whether or not undesired emission was being blocked, depending on whether the target continued to emit after the implosion had occurred.

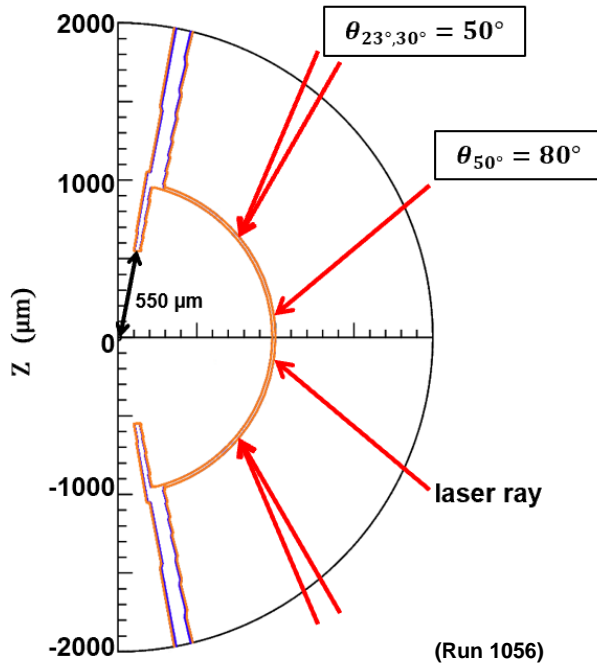


Figure 5.1: The parameters that were adjusted in order to optimize the cone-in-shell design [compare to Fig. 3.1 (a)].

took for the equatorial material (which now received less drive) to reach the center and travel up and down the vertical axis, allowing the cone to converge onto the axis before the hot compressed material could escape. The re-pointing also increased the force driving the polar parts of the shell toward the target center. This inward force opposes the outward flow of compressed material from the cone tip, consequently producing the same effect.

Density contour plots of the new target (Fig. 5.2) showed no hot plasma in the cone after the implosion due to its earlier closing. The absence of contours below the critical density inside the cone, in contrast to the initial design in Fig. 3.4 (b), indicates clearly that no compressed material escaped into the cone. This suggests that no x-ray emission would be detected at this time.

Fig. 5.1 shows the optimized design and the key parameter changes from the initial design [Fig. 3.1 (a)]. The distance from cone tip to target center was increased from 350  $\mu\text{m}$  to 550  $\mu\text{m}$  and the theta pointings of the 23° and 30° beams were decreased from 60° to 50°. The pointings of the 50° beams were not adjusted in order to maintain sufficient drive at the equator. All beams remained in best focus.

It was found that capsules with a greater distance from cone tip to target center minimized the cone's obstruction of the implosion and extended the time it took for the hot plasma to flow to the cone tip, thus allowing the cone tip more time to converge onto the axis. Similarly, a decreased re-pointing of the 23° and 30° beams increased the time it

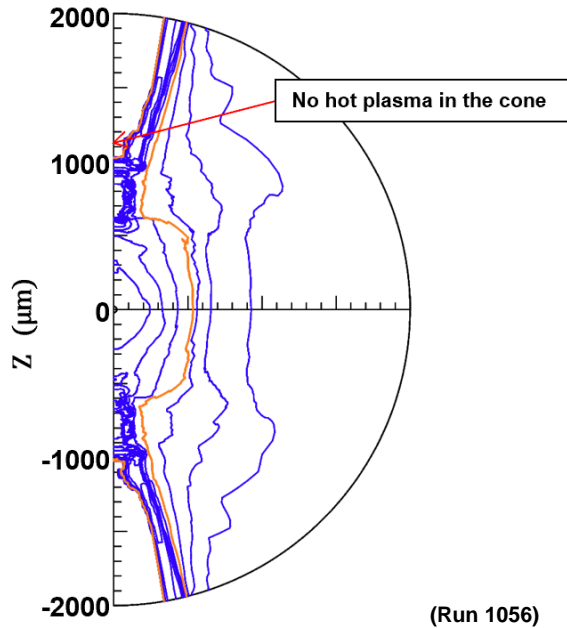


*Figure 5.2: Late stage ( $t=3$  ns) density contour blowup for the new design. The optimized parameters have led the cone to converge onto the vertical axis.*

are a positive velocity and fairly high temperature that extend to  $z\sim 2000$   $\mu\text{m}$  as well as a relatively high density beyond  $1000$   $\mu\text{m}$ , suggesting the presence of a hot, expanding plasma as seen in Fig. 3.4 (b). In contrast, the optimized design [Fig. 5.3 (b)] has no significant plasma past  $z\sim 1000$   $\mu\text{m}$ . This is consistent with the cone converging at  $z\sim 1000$   $\mu\text{m}$  and stopping the expanding implosion material.

Together, the density contour plot and the one-dimensional lineouts suggest that the issue of hot plasma in the cone at late stages has been resolved in the optimized design.

Parts of the cone (indicated by the compact distribution of blue density contours close to the axis from  $z=600$   $\mu\text{m}$  to  $1000$   $\mu\text{m}$ ) appear open, but the tip itself and higher portions of the cone (at  $z\sim 1000$   $\mu\text{m}$ ) have converged onto the axis. While some hot plasma has escaped through the tip, it cannot emit through the cold and dense cone material at  $z\sim 1000$   $\mu\text{m}$ . It is possible to ensure that the convergence occurs sooner by decreasing the radius of the tip, but this would also drastically limit the amount of x-ray emission.

One-dimensional lineouts of density, velocity, and temperature along the vertical axis of Fig. 5.2 at the corresponding time of 3 ns are shown for both the initial and optimized designs in Fig. 5.3. In the initial design [Fig. 5.3 (a)], there

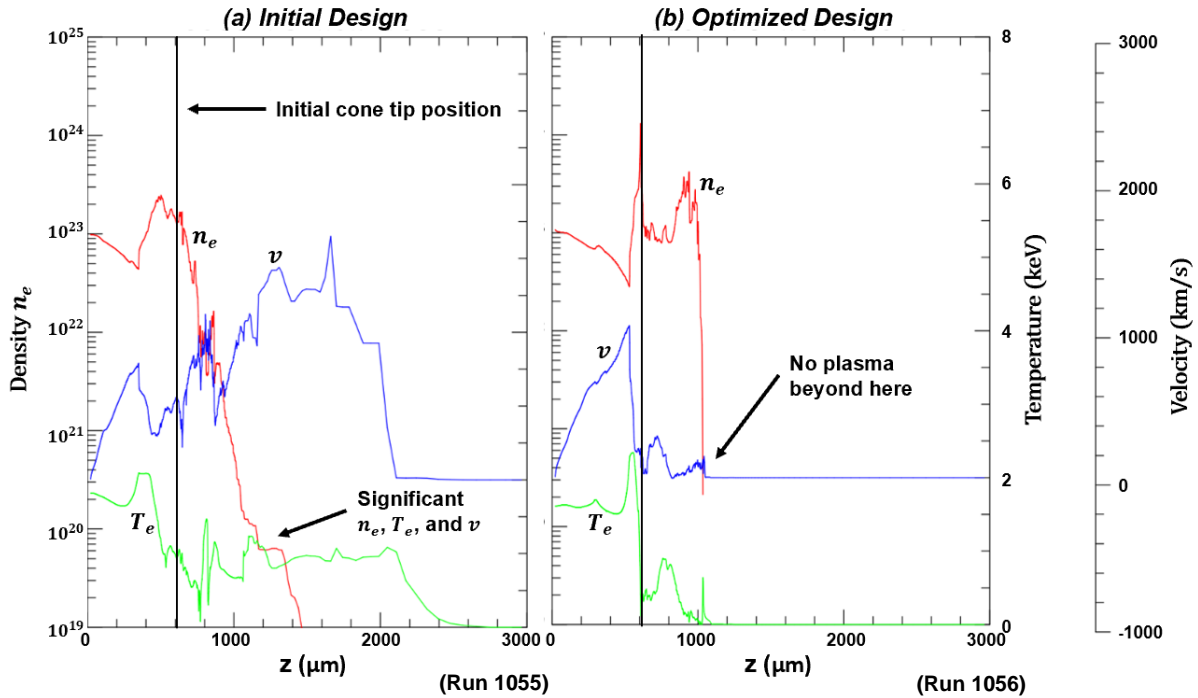


Figure 5.3: One-dimensional lineouts at  $t=3$  ns along the  $z$ -axis for electron density ( $n_e$ , red), velocity ( $v$ , blue) and electron temperature ( $T_e$ , green) for the initial (a) and optimized (b) designs. The sharp drop off in density and temperature as well as the absence of a non-zero velocity past  $1000 \mu\text{m}$  in (b) indicates the lack of an expanding, hot plasma inside of the cone, in contrast to the initial design (a).

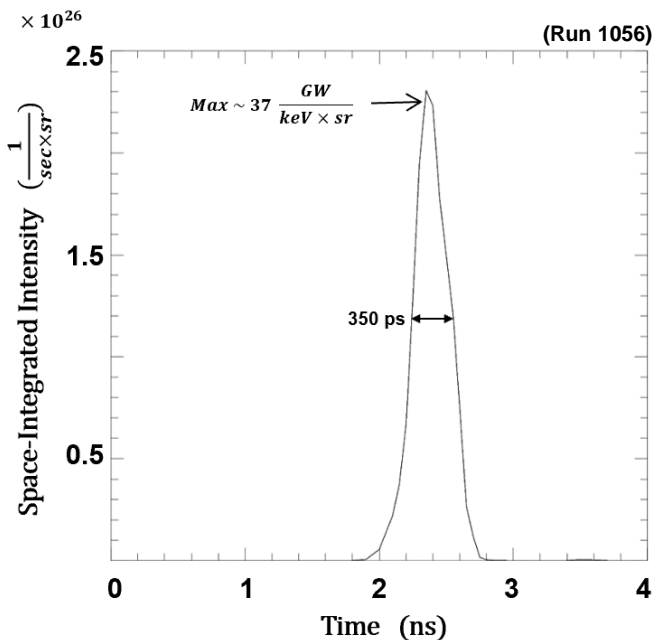


Figure 5.4: Plot of space-integrated intensity versus time for the optimized design. The optimized design produces a short, 350 ps pulse.

An Orion plot of space-integrated intensity versus time for the optimized design (Fig. 5.4) clearly shows how the elimination of late-stage hot plasma in the cone affects x-ray emission: a short, 350 ps x-ray pulse is achieved in the optimized design, contrasting the extended pulse in the initial design (Fig. 4.2). Fig. 5.4 highlights two key features of the optimized design: the lack of run-in emission prior to the implosion and the elimination of post-implosion emission. The first feature, which represents the original purpose of the cones, is also observable in the initial design, but the second is not. The post-implosion emission

that characterized the initial design (Fig. 4.2) is very noticeably not present in the optimized design, and indicates the success of the cone's convergence in sealing off x-ray emission. Together, these differences lead to a short-pulse source of x rays with no run-in emission, which is the primary purpose of the cone-in-shell design.

### 5.2. Comparisons to Conventional Backlighters

In order to better illustrate the advantages of a cone-in-shell backlighter, x-ray output calculations were also carried out for a conventional capsule lacking cones. This design had beam pointings that had been optimized by Y. Yang<sup>12</sup> in order to create a highly uniform implosion. As evidenced by the plot of spatial integral of intensity versus time in Fig. 5.5, the conventional capsule produces a longer pulse with significant run-in when compared to the cone-in-shell design (Fig. 5.4). The duration of the pulse is 600 ps, almost twice as long for the design lacking cones, and there is clearly late-stage emission that is present as late as 4 ns.

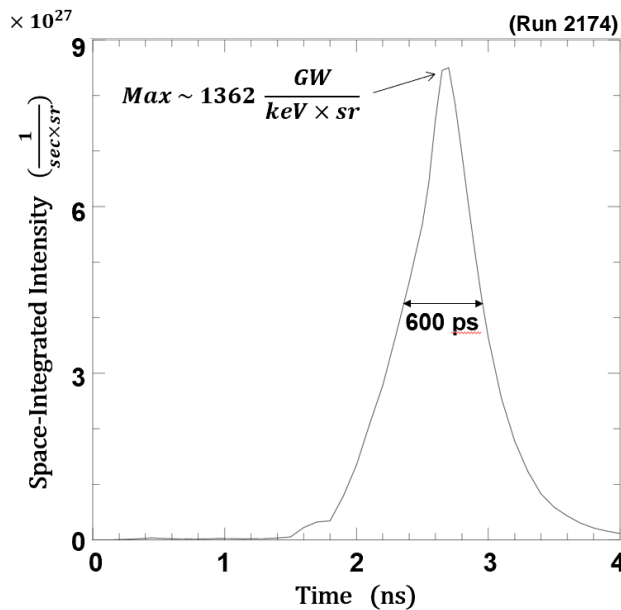


Figure 5.5: Plot of space-integrated intensity versus time for the design lacking cones. Note the extended duration of the pulse as compared to the optimized cone-in-shell design in Figure 5.4.

since there is no cone present to block the x rays.

The output intensities of x rays passing through the target can be temporally integrated to determine the total emission from different positions (x values) over some timespan, allowing the source size to be determined. The time-integrated intensity is defined as

$$\int_0^{t_{\max}} \hat{I}_v dt \quad (8)$$

The cone-in-shell design produces far less emission overall:  $37 \frac{GW}{keV \times sr}$  compared to  $1362 \frac{GW}{keV \times sr}$  in the conventional design, suggesting that the conventional design produces 37 times more emission during the implosion than the cone-in-shell design. This is caused by two main factors. First, the cone-in-shell design produces virtually all of its detectable emission over a 100  $\mu\text{m}$  radius due to the narrow cone tip. The cone tip cannot be enlarged, as this would hinder the cone's ability to converge on the axis in order to prevent late-stage emission. In contrast, the conventional design produces emission over the entire 400  $\mu\text{m}$  radius of the collimator

where  $\hat{I}_\nu$  is the spectral intensity as previously defined and  $t$  is time. The upper bound of the integral  $t_{max}$  is 4 ns in order to include emission before, during, and after the peak compression, all of which contribute to the spectrometer's measurements. Fig. 5.4 and Fig. 5.5 show that there is negligible emission at  $t_{max}$ . Since the integral is over time, its units are  $\frac{1}{sr \times cm^2}$ .

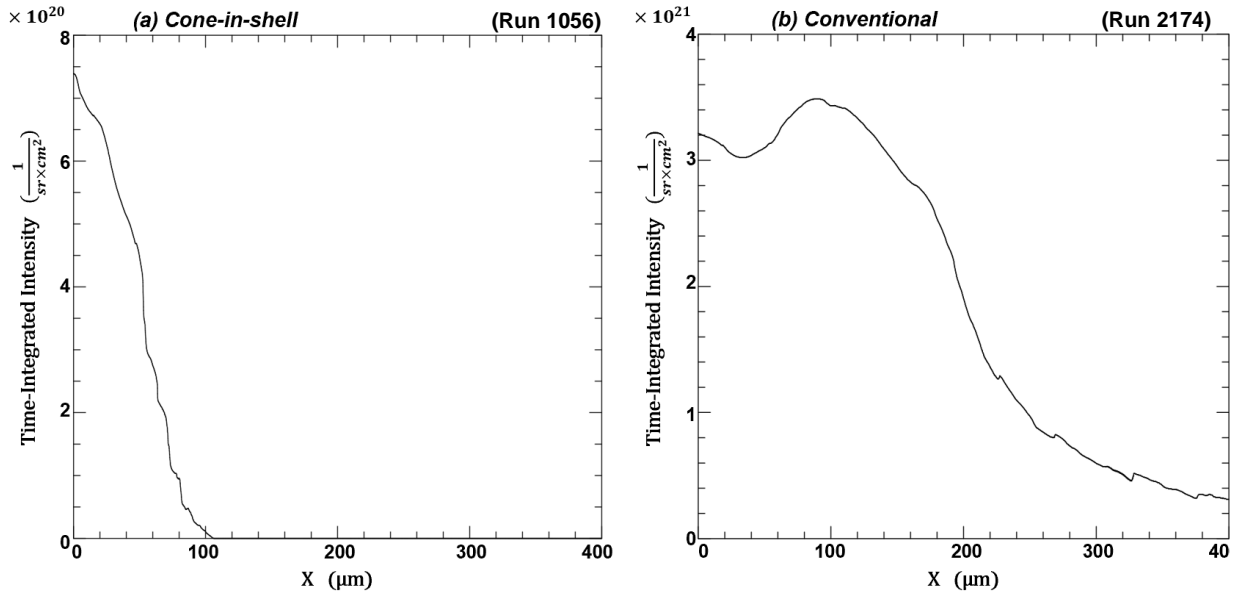


Figure 5.6: Plots of time-integrated intensity versus position for the cone-in-shell (a) and conventional (b) designs. Note the significantly wider radius from which emission is detected for the conventional design as compared to the cone-in-shell design.

Plots of the time-integrated intensities for the two designs, shown in Fig. 5.6, illustrate the difference in source size. The conventional design has a significantly larger radius from which emission is available. This four-fold increase in radius translates to a sixteen-fold increase in area, a factor that would be directly reflected when integrating over space to determine the total emission.

Second, it is not possible to achieve the same quality of implosion for a cone-in-shell design as there is no polar material to implode. This limits the densities and temperatures that can be reached at peak compression, further decreasing the x-ray output. The difference in quality of implosion can be observed by comparing the central emission from the two targets. In Fig. 5.6 (a), the central emission (at  $x=0$ ) is  $\sim 7.5 \times 10^{20} \frac{1}{sr \times cm^2}$ , whereas in Fig. 5.6 (b), the emission at the same point is  $\sim 3.2 \times 10^{21} \frac{1}{sr \times cm^2}$ , a factor of 4.3 higher. This difference is much smaller than the factor of 16 that distinguishes the two areas of emission.

These two factors explain the majority of the difference in maximum x-ray emission seen in the plots of space-integrated intensity (Fig. 5.4 and Fig. 5.5). The cone-in-shell target can produce the desired short pulse of x rays, but at the cost of a reduced signal as compared to a conventional backlighter.

## 6. Conclusion

In this work, a double cone-in-shell backlighter was optimized using the 2D hydrodynamics code *SAGE* and the x-ray diagnostic code *Orion*, which was developed to aid in the prediction of emission from imploding targets. The capsule was optimized to produce a short, 350 ps pulse of x rays for the backlighting of Fe opacity experiments at the NIF. The design eliminates undesired run-in produced by current backlighters. The optimized convergence of the cone on the vertical axis following the implosion prevents contributions from emission produced after peak compression.

This design could allow for significantly improved opacity measurements, offering insight into the question of the solar radiative-convective transition radius. *Orion* is able to guide the further development of this backlighter on the NIF.

## 7. Acknowledgements

I would like to thank Dr. Heeter for providing me with information on the NIF opacity platform as well as feedback on my cone-in-shell design. I would also like to thank Yujia Yang for providing me with optimized beam pointings for a conventional capsule. Finally, I would like to thank Dr. Craxton for his invaluable assistance throughout my project and the incredible opportunity to participate in the high school program.

## 8. References

1. R. F. Heeter et al., “Conceptual Design of Initial Opacity Experiments on the National Ignition Facility,” *J. Plasma Phys.* **83**, 595830103 (2017).
2. J. Nuckolls et al., “Laser Compression of Matter to Super-High Densities: Thermonuclear (CTR) Applications,” *Nature* **239**, 139 (1972).
3. R. S. Craxton et al., “Direct-Drive Inertial Confinement Fusion: A Review,” *Phys. Plasmas* **22**, 110501 (2015).
4. J. D. Lindl, “Development of the Indirect-Drive Approach to Inertial Confinement Fusion and the Target Basis for Ignition and Gain,” *Phys. Plasmas* **2**, 3933 (1995).
5. T. R. Boehly et al., “Initial Performance Results of the OMEGA Laser System,” *Opt. Commun.* **133**, 495 (1997).
6. S. Skupsky et al., “Polar Direct Drive on the National Ignition Facility,” *Phys. Plasmas* **11**, 2763 (2004).
7. A. M. Cok et al., “Polar-Driven Designs for Optimizing Neutron Yields on the National Ignition Facility,” *Phys. Plasmas* **15**, 082705 (2008).
8. Y. P. Opachich et al., “Capsule Implosions for Continuum X-ray Backlighting of Opacity Samples at the National Ignition Facility,” *Phys. Plasmas* **24**, 063301 (2017).
9. R. F. Heeter, Lawrence Livermore National Laboratory, private communication (2018).
10. R. Kodama et al., “Fast Heating of Ultrahigh-Density Plasma as a Step Towards Laser Fusion Ignition,” *Nature* **412**, 798 (2001).
11. Ya. B. Zel’dovich and Yu. P. Raizer, “Physics of Shock Waves and High-Temperature Hydrodynamic Phenomena,” Academic Press Inc. (1967).
12. Y. Yang, Laboratory for Laser Energetics, private communication (2018).